Transactions of Materials Research 1 (2025) 100010

Contents lists available at ScienceDirect

Transactions of Materials Research

journal homepage: www.sciencedirect.com/journal/transactions-of-materials-research

Developing graphene oxide@In-Bi alloy composite via layer-by-layer strategy achieving efficient heat dissipation towards thermal interfacial applications

Yifan Li [a], Junhui Fan [a], Changqing Liu [b], Dahai Zhu [a], Chen Jiang [a], Wei Yu [a,*]

[a] School of Energy and Materials, Shanghai Polytechnic University, Shanghai, 201209, China
[b] School of Mechanical and Energy Engineering, Shaoyang University, Shaoyang, Hunan, 422001, China

ARTICLE INFO

Keywords:
Thermal interface material
Liquid alloy
Thermal contact resistance

ABSTRACT

We develop a graphene oxide (GO)@In-Bi alloy composite that exhibits flexibility, leak-proof properties, and efficient interfacial heat transfer. This composite was fabricated using a layer-by-layer strategy for applications in thermal interface materials (TIMs). The incorporation of liquid metal with high thermal conductivity enhances the cross-plane thermal conductivity of the GO film to 1.35 W/(m · K) while reducing the thermal contact resistance to 0.47 °C cm^2/W. Upon exposure to high-temperature conditions, the In-Bi phase transition occurs, filling the gaps between rough interfaces and facilitating interface wetting, thereby improving heat transfer efficiency. Additionally, due to surface tension effects, the liquid alloy evenly coats the GO surface, providing the composite film with robust mechanical properties and ensuring excellent leak resistance. Overall, this study presents a novel approach for fabricating flexible liquid alloy-based composites with high thermal conductivity and low thermal contact resistance, providing fresh perspectives on the synthesis of TIMs.

1. Introduction

Thermal interface materials (TIMs) play a crucial role in enhancing heat dissipation and thermal management in various electronic and optoelectronic devices [1]. With the continuous miniaturization and increasing power density of these devices, efficient heat transfer across interfaces become paramount to ensure optimal performance, reliability, and longevity [2]. TIMs serve as bridges between heat-generating components and heat sinks, facilitating the efficient transfer of heat away from critical areas [3].

From materials perspectives, traditional TIMs are commonly classified into three categories: solid, paste, and liquid forms [4]. Solid TIMs typically exhibit high mechanical strength and stability, maintaining their shape even under high pressure or extrusion [5]. They resist flow and volatilization, offering reliable heat dissipation for applications with elevated temperatures and high-power densities. Nonetheless, solid TIMs often entail a large thermal resistance between themselves and the contact surface, resulting in suboptimal heat transfer efficiency. Moreover, they demand stringent requirements for contact pressure and surface flatness during assembly. Solid TIMs mainly include metal sheets (such as copper or aluminum), ceramic sheets, and thermally conductive silicon pads. Paste TIMs can effectively fill small gaps and irregularities, enhancing the contact area of the thermal interface surface and consequently improving heat transfer efficiency [6]. They are typically easy to apply and assemble. However, the liquid component may evaporate over time, compromising their thermal performance. Carbon-based and metal-based thermal conductivity pastes are commonly employed in this category. Liquid TIMs have the advantage of filling minute gaps on the contact surface, leading to a significant increase in thermal contact area and heat transfer efficiency [7]. However, they may exhibit volatility over prolonged use, resulting in diminished effectiveness. Examples of liquid TIMs include thermal silicone oil, thermal grease, and thermal liquid metal (such as gallium and indium). Each type of TIM has its unique advantages and suitability for various application scenarios. The selection of the appropriate TIM depends on the specific thermal management requirements, budget constraints, and available space in a given application [8].

In recent years, phase-change thermal interface materials (PCTIMs), which integrate phase change and heat conduction, have emerged as a focal point of research in electronic device heat dissipation. At ambient temperatures, their solid state ensures robust mechanical strength and stability. However, during elevated temperatures, phase transition en-

* Corresponding author.
E-mail address: yuwei@sspu.edu.cn (W. Yu).

https://doi.org/10.1016/j.tramat.2025.100010
Received 2 April 2025; Received in revised form 5 April 2025; Accepted 6 April 2025
Available online 9 April 2025
3050-9149/© 2025 The Authors. Published by Elsevier B.V. on behalf of Chinese Materials Research Society. This is an open access article under the CC BY license (http://creativecommons.org/licenses/by/4.0/).

sures sufficient interface contact, thereby markedly enhancing heat transfer efficiency [9]. Currently, there have been theoretical and experimental investigations on PCTIMs for managing the interfacial heat dissipation of electronic devices. Zhou et al. synthesized composite materials using polydimethylsiloxane (PDMS) incorporating paraffin@SiO_2 nanocapsules and developed a physical model inspired by prevalent computer CPU cooling systems [10]. They demonstrated the influence of capsule melting point and enthalpy on the chip heating rates. Zhao et al. incorporated vertically aligned short carbon fibers into the blend of silicone rubber and paraffin wax to fabricate a phase change thermal pad with a stable form. This composite exhibits a thermal conductivity of 7.00 W/(m · K) and reduces thermal impedance by 54.4 % during the phase change process [11]. They also attempted to fabricate a thermal pad by blending a low-melting-point alloy (62.5Ga21.5In16Sn) with expanded graphite. This composite exhibits a thermal conductivity of 26.94 W/(m · K) and achieves a remarkably low thermal impedance of 0.42 K cm^2/W. Moreover, the cooling efficiency under forced air convection surpasses that of commercial thermal pads by 36.78 % [12]. These mentioned cases represent mainstream PCTIM categories: microencapsulated PCM, nanocomposite films, and liquid metal-based PCM. Microencapsulated PCM typically demonstrates stable phase transition and excellent leak resistance. However, its material composition is intricate, posing challenges in preparation and performance control. Nano-composite membranes exhibit favorable contact characteristics and flexibility but often have low thermal conductivity. Liquid metal-based PCM offers high thermal conductivity but is susceptible to leakage issues. Consequently, the design of material components and interface engineering remains a focal point and challenge in developing PCTIMs with optimal thermal conductivity, flexibility, and leak resistance.

In this study, a uniform coating of liquid In-Bi alloy is applied onto the graphene oxide (GO) film surface with a thermally conductive composite film obtained via the layer-by-layer strategy. The surface tension drives the liquid alloy to form a stable thin layer on the GO surface. At ambient temperature, the film exhibits solidity, with the In-Bi alloy coating serving as an adhesive, thereby enhancing the mechanical flexibility and durability. When employed as a TIM between the heat source and the heat sink, the In-Bi alloy liquefies, accompanied by the gaps filled between rough interfaces, consequently reducing thermal contact resistance and facilitating interfacial heat transfer. The developed composite film demonstrates favorable flexibility, high thermal conductivity, and leak prevention, with a straightforward preparation process. Practical thermal management testing proves its favorable exceptional heat dissipation performance functioning as a TIM, underlining its considerable potential for further commercial promotion.

2. Experimental

2.1. Materials

Sulfuric acid (H_2SO_4, 19 mol/L) and sodium nitrate ($NaNO_3$, >98.5 %, AR) were purchased from Aladdin Reagent Shanghai Co., Ltd. Gallium-indium alloy (Ga-In, Ga75-In25) was purchased from Sichuan High Purity Materials Technology Co., Ltd. Indium-bismuth alloy (In-Bi, In66.3-Bi33.7) was purchased from Changsha Kunyong New Materials Co., Ltd. Flake graphite (2–3 μm, ≥99 %), potassium permanganate ($KMnO_4$, ≥99 %, AR), hydrogen peroxide (H_2O_2, >10 %), hydrochloric acid (HCl, 5 %, AR), anhydrous ethanol (AE, >99.8 %, GR) were purchased from Titan Technology Co., Ltd. All chemical reagents were used without further purification.

2.2. Preparation of GO and GO/In-Bi composite film

In the experiment, 3.2 g $NaNO_3$ was dissolved in 46 mL concentrated H_2SO_4 under mechanical stirring. Subsequently, the beaker containing the solution was immersed in an ice bath, stirring continuously for 30 min to ensure thorough mixing. Then, 2 g graphite flakes were incorporated into the mixture, continuing to stir for an additional 45 min; 0.3 g $KMnO_4$ was sequentially added every 3 min until reaching a total of 6 g, closely monitoring to maintain the temperature below 5 °C. Throughout the reaction, the mixture gradually became a purplish-red oily substance. After a total of 60 min of stirring in the ice bath, the reaction vessel was transferred to an oil bath preheated to 40 °C, maintaining stirring for another 90 min. DI water of 92 mL was gently introduced before relocating the reactor to a 100 °C oil bath for 15 min. The reactor was removed and cooled to about 60 °C, followed by gradually adding 180 mL DI water for a continuous cooling process. A 30 mL H_2O_2 solution was carefully incorporated until no further bubbles emerged. The color of the solution gradually switched from brown to golden. After the solution was settled down for 12 h, it was centrifuged at 4500 RPM to obtain the GO filter cake. The cake was cleaned with a 5 % hydrochloric acid solution followed by five washes in DI water until the pH of the solution was stable at 7.

GO was homogeneously mixed with DI water in an appropriate ratio, achieving dispersion following 12 h of ultrasonic treatment. A uniform film was then formed by spreading a specified volume of this dispersion onto a plate with a coater and subsequently drying it in an oven at 60 °C for 3 h. This film was placed on a heating table maintained at 80 °C, and subjected to hot pressing for 5 min before In-Bi alloy particles were distributed on the film surface. Once the alloy melted, a plastic brush was employed to uniformly coat both sides of the film, ensuring even coverage. Upon cooling, a GO@In-Bi composite film was fabricated. For comparison, another composite film was also fabricated by the alloy onto the GO film without the hot-pressing step. Additionally, GO@Ga-In composite films were similarly prepared to explore the impacts of varying alloy compositions on interfacial heat conduction. The fabrication process for both the GO film and the GO@In-Bi composite film is illustrated in Fig. 1a. The heat-treated and non-heat-treated GO films are denoted as GO_w and $GO_{w/o}$, respectively. It is noteworthy that conventional In-Bi films lack the capability of restoration post-heating, rendering them unsuitable for direct applications as TIMs, as shown in Fig. 1b. Conversely, the GO_w@In-Bi composite film retains its restorative properties after heating. This phenomenon primarily stems from the amalgamation of liquid metal with the graphene film, wherein the liquid metal establishes a stable thin layer on the graphene film's surface. Consequently, owing to surface tension, the liquid metal uniformly disperses across the surface of GO, engendering a cohesive coating that effectively mitigates leakage.

2.3. Characterizations

The micromorphology was characterized using a scanning electron microscope (SEM, Hitachi S-4800, Japan) with the acceleration voltage of 20 kV. The microstructure was studied by X-ray diffraction (XRD, Brugge D8-Advance, Germany) under 40 mA and 40 kV with a scanning rate of 5°(2θ)/min. The optical properties and bonding situations were analyzed using a UV–visible spectrophotometer (PerkinElmer, USA). The energy distribution of emitted photoelectrons and surface Auger electrons was tested using an X-ray photoelectron spectrometer (XPS, ESCALAB 250Xi). The thermal conductivity was measured using a thermal conductivity meter (C-THERM TCi, Canada). Mechanical properties were tested using a universal electronic testing machine (MTS, CMT6103, China). The specimens used for the test were rectangular in shape with dimensions of 5.08 cm × 1.27 cm. The thermal stability was studied by thermal gravimetric analysis (TGA, NETZSCH, Germany, STA 449F5) from room temperature to 800 °C at a rate of 10 °C/min under a nitrogen atmosphere. The nitrogen flow rate was 20 mL/min. Infrared thermal images were captured using the FLIR (USA, T640). The thermal resistance was tested through a contact thermal resistance testing machine (LW-9389, Longwei Technology Co., Ltd., Taiwan, complying with ASTM-D5470 standard). The tested thermal resistance consists of the thermal resistance of the TIMs and the thermal contact resistance (TCR).

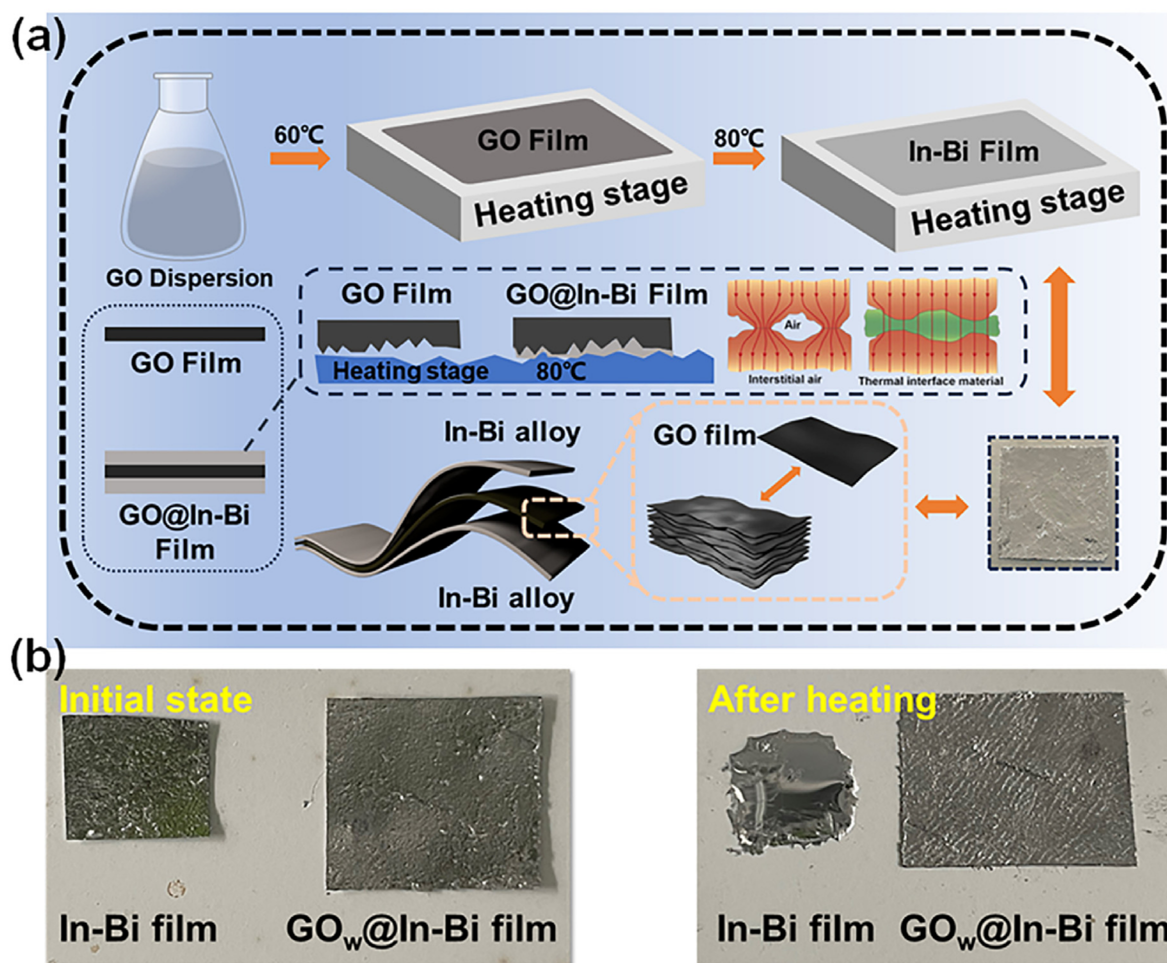

Fig. 1. (a) Schematic diagram of the preparation of GO film and GO@In-Bi film; (b) surface morphological change of GO film and GO_w@In-Bi film before and after heating (the original size of GO film and GO_w@In-Bi is around 2.5 × 2.5 cm and 3.5 × 3.5 cm, respectively).

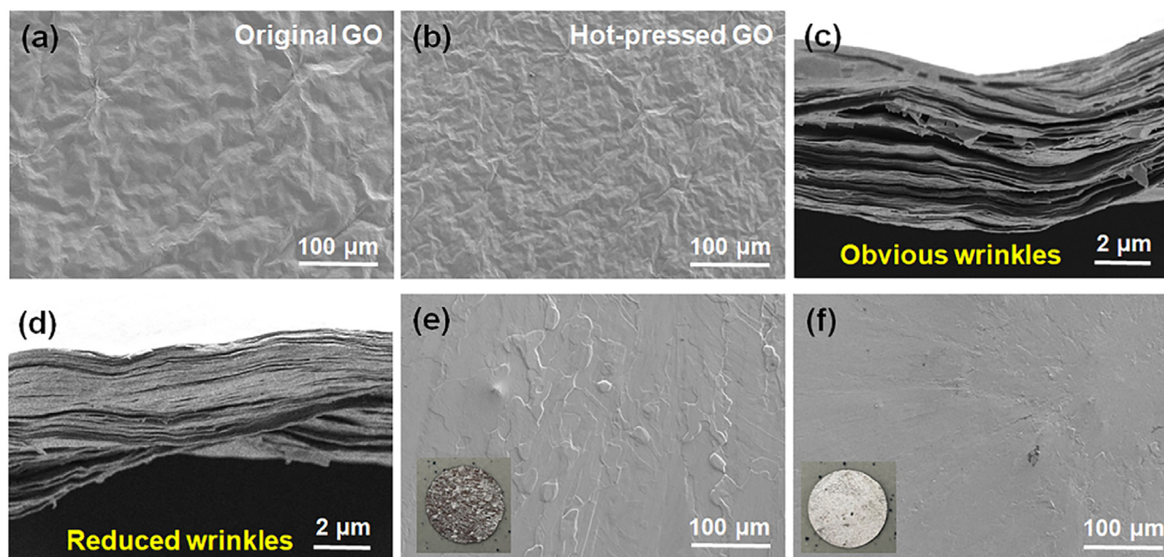

Fig. 2. Surface SEM images of (a) $GO_{w/o}$ and (b) GO_w film; crossection SEM images of (c) $GO_{w/o}$ and (d) GO_w film; surface SEM images of the (e) $GO_{w/o}$@In-Bi film and (f) GO_w@In-Bi film.

3. Results and discussions

3.1. Micromorphology and structure characterizations

The influence of the hot-pressing treatment on the micromorphology change of the film is first studied. Fig. 2a and b compare the surface SEM images of GO films before and after hot pressing. Obvious wrinkles are observed in $GO_{w/o}$ film, which are usually considered thermal barrier areas [13]. Post-treatment, the films show a higher density of folds with reduced peak heights, facilitating more effective surface contact [14]. Additionally, the cross-sectional SEM images confirm tighter adhesion and reduced layer spacing between the GO film layers after hot pressing, enhancing the directionality of heat transfer efficiency, as shown in Fig. 2c and d. In addition, the surface morphology of GO_w@In-Bi composite films is studied, and the results are shown in Fig. 2e and f. They exhibit significantly lower surface roughness compared to GO films, in the absence of noticeable wrinkles. This smoother surface achieved through hot pressing ensures lower interface TCR, making the composite films particularly effective as TIMs.

The structural characteristics of the films are analyzed by XRD, as shown in Fig. 3a. The analysis identifies the distinct characteristic peak of GO at 11.68°, associated with the (002) diffraction plane [15]. For the GO_w@In-Bi composite, characteristic peaks of the In-Bi alloy are observed at 27.32°, 47.36°, and 56.09°, aligning with the (100), (110), and (200) diffraction planes, respectively [16]. The clarity of these peaks suggests that the layer-by-layer process preserves the internal structure of the composite. XPS is employed to analyze the molecular structure and valence states of the surface of the GO_w film and the GO_w@In-Bi composite film with the results shown in Fig. 3b–f. The peaks observed at 285.1 eV, 532.1 eV, 161.1 eV, and 444.1 eV correspond to C 1s, O 1s, Bi 4f, and In 3d, respectively [17]. Further chemical state analysis of C and O in GO is provided in Fig. 3c and d. Within the primary peak of O 1s, the deconvoluted peaks at 531.8 eV and 530 eV signify C-O and C=O bonds, respectively. Similarly, within the primary peak of C 1s, the four deconvoluted peaks at 282.9 eV, 283.9 eV, 286.1 eV, and 288.1 eV correspond to C=C, C-C, C-O, and C=O bonds, respectively [18]. For GO_w@In-Bi, the peaks at 443.3 eV and 450.9 eV correspond to In $3d_{5/2}$ (metal) and In $3d_{3/2}$ (metal), Fig. 3e. Additionally, deconvoluted peaks In $3d_{5/2}$ (O) and In $3d_{3/2}$ (O) are observed at 444.3 eV and 452 eV, indicating the oxidation of In in the alloy. Likewise, the peaks observed at 155.4 eV and 160.7 eV correspond to two characteristic peaks of Bi element: Bi $4f_{7/2}$ (metal) and Bi $4f_{5/2}$ (metal), Fig. 3f. The observed deconvoluted peaks of Bi $4f_{7/2}$ (O) and Bi $4f_{5/2}$ (O) suggest oxidation of Bi. This oxidation may occur due to the formation of molten metal during the composite process with GO, thus demonstrating good compatibility between the two materials [19].

3.2. Optical, mechanical, and hydrophilic properties characterizations

The optical characteristics of the GO_w film and the GO_w@In-Bi composite film are evaluated, with findings presented in Fig. 4a. It is observed that the GO_w@In-Bi composite film exhibits significantly reduced absorption within the wavelength range 400–800 nm. The decreased absorption is attributed to the incorporation of the In-Bi alloy, which imparts a distinct silver hue to the composite film, as shown in the inserted digital image. Conversely, the surface of the GO_w film displays a dark brown coloration, and it exhibits a high absorption rate across the 200–800 nm wavelength spectrum, achieving values exceeding 0.9.

The load-bearing capacity of the film is evaluated, as presented in Fig. 4b. The GO_w film without In-Bi alloy coated could support a maximum weight of 200 g before succumbing to failure. In contrast, the composite film fabricated using a layer-by-layer approach demonstrates the ability to sustain a load of 400 g. Tensile testing further corroborated the superior mechanical properties of the GO_w@In-Bi composite film, indicating fracture stress of 1170.9 kPa, which is approximately 120.8 % higher than that of the GO_w film (530.3 kPa), Fig. 4c. Moreover, the incorporation of a highly malleable liquid metal endows the composite film with enhanced flexibility, enabling it to be bent into various configurations and to regain its original shape over time, Fig. 4d. This remarkable ability to adapt its shape significantly augments the contact adequacy when employed as a TIM, thereby facilitating improved heat transfer performance at the interface.

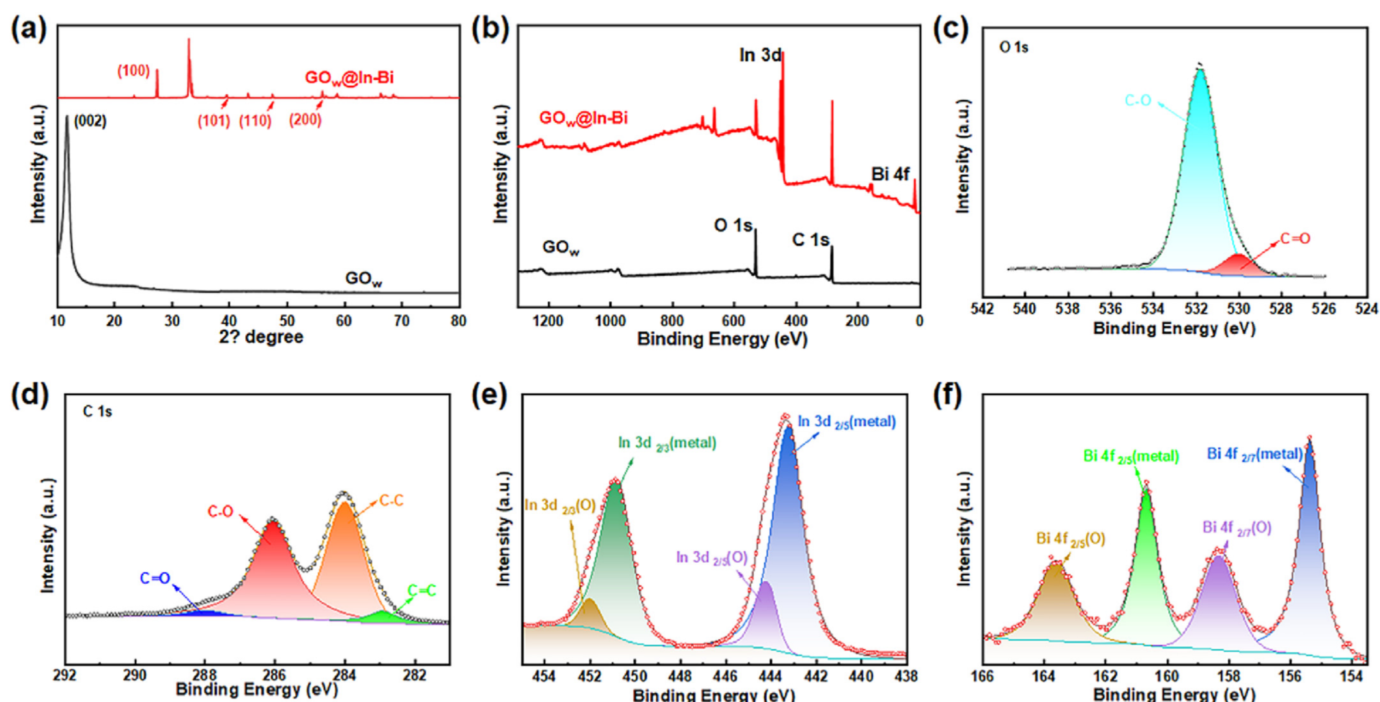

Fig. 3. (a) XRD spectra of GO_w and GO_w@In-Bi films; (b) wide-scan XPS curves of GO_w and GO_w@In-Bi films; (c–d) O 1*s* and C 1*s* XPS spectra of GO_w film; (e–f) In 3*d* and Bi 4*f* XPS spectra of GO_w@In-Bi film.

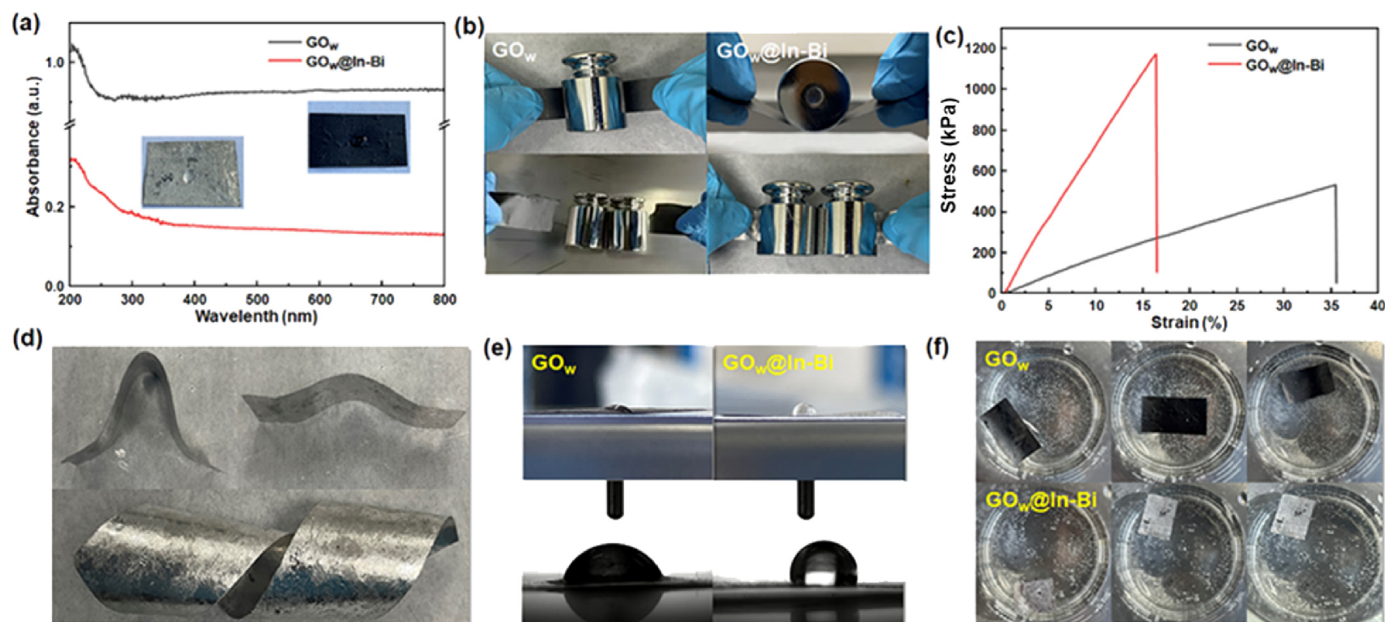

Fig. 4. (a) The absorption spectra of the GO_w and GO_w@In-Bi composite film in the 200–800 nm wavelength range; (b) load-bearing capacity test of GO_w and GO_w@In-Bi composite films; (c) stress-strain curves of GO_w and GO_w@In-Bi composite films; (d) flexibility test of GO_w@In-Bi composite films; (e) hydrophobic angle test of GO_w and GO_w@In-Bi composite films; (f) waterproof resistance test of GO_w and GO_w@In-Bi composite films.

The contact angle of the film is measured with the results shown in Fig. 4e. There are abundant hydrophilic oxygen-containing functional groups on the surface of GO_w film, and water droplets are quickly adsorbed when in contact with water. A contact angle of 69° is observed, indicating its good hydrophilicity. This characteristic predisposes the TIMs to create a humid environment upon water absorption, potentially accelerating corrosion on the contact metal surfaces. Moreover, the hydrophilic nature may prompt physical or chemical alterations (e.g., expansion, softening, or decomposition), adversely impacting its heat transfer efficacy and mechanical integrity. Conversely, the GO_w@In-Bi composite film exhibits a contact angle of 136°, reflective of notable hydrophobic properties. This hydrophobicity may stem from the lowered surface energy of the composite system, a result of the synergistic effect between the liquid metal and GO, enhancing the long-term stability of the TIM. Water contact experiments performed on both films are presented in Fig. 4f. Initially, the GO_w film remains afloat on water but eventually sinks and slightly expands. In contrast, the GO_w@In-Bi film neither swells nor sinks when submerged in water for the same duration owing to its hydrophobic qualities.

3.3. *Thermal characterizations*

The thermal stability of the GO_w and GO_w@In-Bi composite films is evaluated with the TGA curve presented in Fig. 5a. The mass loss of the GO film reaches 50 % upon heating to 800 °C, whereas the GO_w@In-Bi film exhibits only a 7.2 % loss. The plenty of oxygen-containing functional in GO decomposes between 150 and 200 °C, producing significant amounts of gas and heat, leading to pressure increases [20]. The rapid expansion of GO occurs when the pressure surpasses the van der Waals forces, resulting in the splattering of samples and the formation of ash [21]. Conversely, liquid metals typically possess a high specific heat capacity, thereby slowing the rate of temperature increase of the composite film under thermal load [22]. Additionally, the high thermal conductivity of the liquid metal enhances the overall heat transfer, and the robust interface between GO and In-Bi (reflected by previous mechanical characterization) reduces the inside thermal resistance and prevents heat accumulation, both of which significantly contribute to the enhanced thermal stability of the film. Furthermore, the inserted DTG curve in Fig. 5a indicates that both GO and GO_w@In-Bi exhibit peak weight loss rates at approximately 200 °C, attributed to the decarboxylation of the -COOH groups [23]. The weight loss rate for GO_w@In-Bi film is −0.5 %/min, markedly lower than the −5.07/min observed for GO film. This comparison substantiates that the incorporation of liquid metal markedly boosts the thermal stability of the film.

The thermal conductivity of the film is initially tested to determine the impact of In-Bi alloy on heat transfer, with results presented in Fig. 5b (cross-plane direction) and Fig. 5c (in-plane direction). The hot-pressing treatment enhances the packing density between layers, reducing cross-layer thermal resistance and consequently increasing thermal conductivity [24]. GO_w@In-Bi exhibits a higher cross-plane thermal conductivity of 1.35 W/(m·K), more than twice that of GO_w (0.44 W/(m·K)). This substantial increase can be attributed to the introduced In-Bi alloy significantly enhancing the density of the GO film with an almost unchanged thermal diffusion coefficient. Since the structural alignment within the plane remains largely unchanged, the in-plane thermal conductivity of GO_w@In-Bi is almost equal to that of GO_w.

Thermal resistance is a critical factor for evaluating the heat transfer performance of TIMs [25]. The testing principles of TCR are shown in the Supporting Information. The TCR values of the film under various temperature and pressure conditions are tested, with the results shown in Fig. 5d and e. Fig. 5d illustrates the TCR change of the film under different temperature gradients at the pressure of 30 psi. The TCR of the $GO_{w/o}$ is the highest, reaching 6.59 °C cm^2/W at 40 °C. In comparison, the TCR of $GO_{w/o}$@In-Bi and $GO_{w/o}$@Ga-In films are 2.45 °C cm^2/W and 3.99 °C cm^2/W at 40 °C, respectively. Notably, the TCR of $GO_{w/o}$@In-Bi film shows a significant decrease during the transition from 70 °C to 80 °C. This sharp reduction is attributed to the phase transition from solid to fluid as the point of the In-Bi alloy is approximately 72 °C, which fills the interfacial gaps and improves the interfacial contact. The TCR of the $GO_{w/o}$ film and $GO_{w/o}$@Ga-In composite film decreases with the increased pressure, Fig. 5e. The increased pressure improves the contact situation and thus reduces the contact resistance. It should be noticed that the decrease in TCR for the $GO_{w/o}$@In-Bi composite film is minimal, indicating that the alloy has already filled most of the gaps at 30 psi, and further pressure has little impact on enhancing interface transfer. Fig. 5f illustrates the TCR change for the GO film and GO@In-Bi composite film

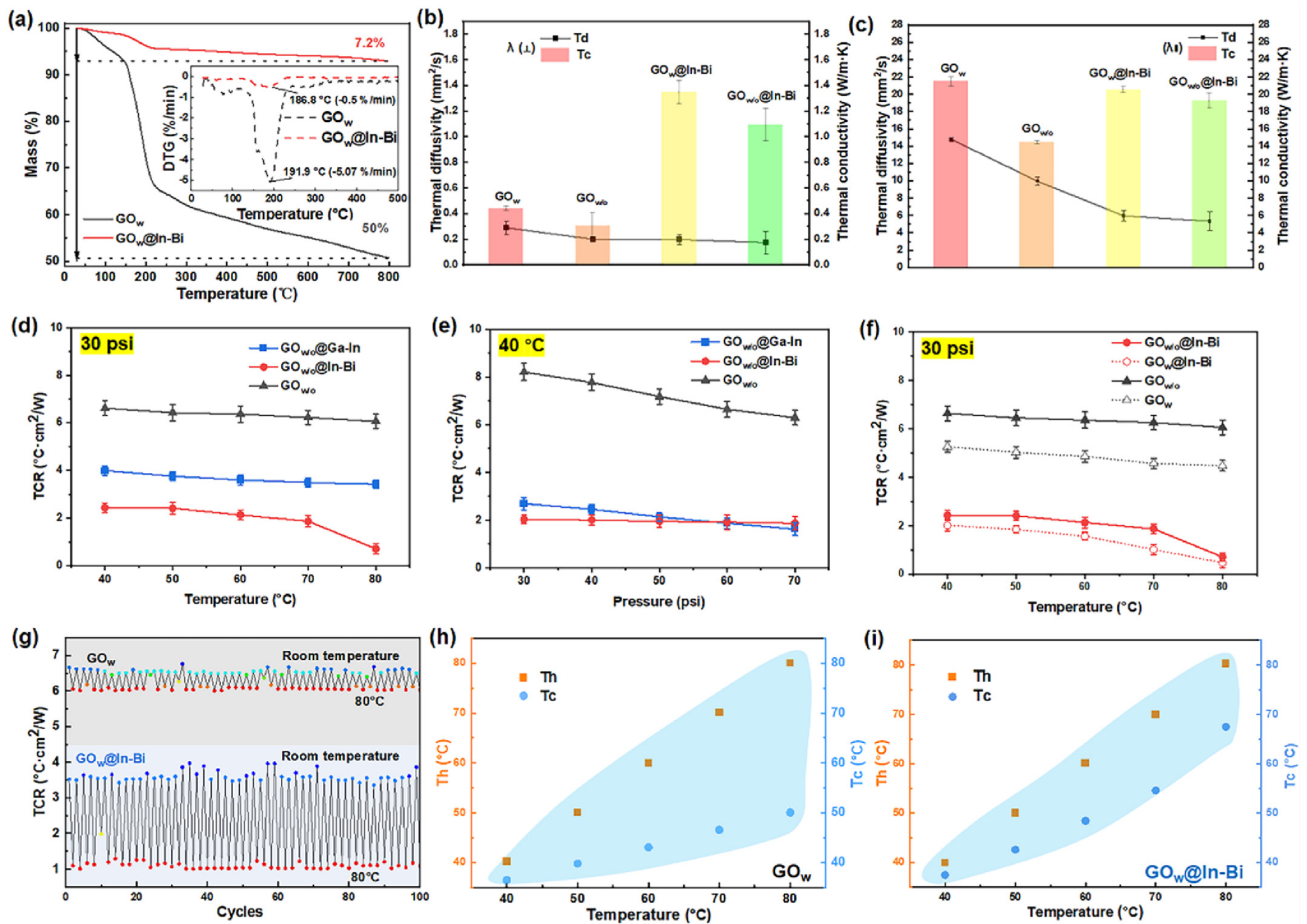

Fig. 5. (a) TGA and DTG curves of GO_w and GO_w@In-Bi; the thermal conductivity of $GO_{w/o}$, GO_w, GO_w@In-Bi, and $GO_{w/o}$@In-Bi at (b) cross-plane direction and (c) in-plane direction; (d, e) TCR comparison of $GO_{w/o}$, $GO_{w/o}$@In-Bi, and $GO_{w/o}$@Ga-In under various temperature and pressure; (f) TCR comparison of GO and GO@In-Bi before and after hot-pressing under different temperature; (g) high and low-temperature TCR cycling test curves of GO_w and GO_w@In-Bi; (h–i) the temperature differential between the hot and cold ends under varying temperature gradients of GO_w and GO_w@In-Bi.

before and after hot pressing. The hot-pressing treatment reduces the TCR of the GO film from 6.59 °C cm^2/W to 5.27 °C cm^2/W. This reduction is attributed to the denser lamellar structure of the latter, which results in smaller interlayer gaps and significantly decreased interface thermal resistance. GO@In-Bi composite film generally exhibits a similar trend, although the magnitude of change is smaller. This is because the composite film has better interface contact than the pure GO film, leading to a smaller reduction in TCR after hot-pressing. The TCR stability of the film after undergoing high and low-temperature cycling is evaluated and the results are shown in Fig. 5g. Both the GO_w and GO_w@In-Bi composite films exhibit robust thermal resistance stability across high and low temperatures. Notably, the TCR of the GO_w@In-Bi composite films decreases significantly, reducing to approximately 0.47 °C cm^2/W at 80 °C. Considering that the TCRs of commercially available thermal greases and thermal pads are approximately 1 °C cm^2/W and 2 °C cm^2/W, respectively, the GO_w@In-Bi composite films developed in this study demonstrate significant potential for practical applications. The instability TCR of GOw@In-Bi is attributed to the uneven distribution of the liquid metal along the vertical direction under heating. Furthermore, the temperature differential between the hot and cold ends under varying temperature gradients is recorded, with results presented in Fig. 5h and i. The circled area indicates the temperature difference between the cold and hot ends. The temperature difference in the GO_w@In-Bi composite film is considerably lower than that in the GO_w film, which is also attributed to reduced thermal resistance.

3.4. Practical thermal management validation

The thermal management performance of the films is evaluated. GO_w and GO_w@In-Bi films are placed on an iron heating plate set at 100 °C. An aluminum heat dissipation fin is employed as the heat sink and the film thickness is around 0.2 mm. The temperature changes are captured using an infrared thermal imager, as illustrated in Fig. 6a. Initially, the temperature of both GO_w and GO_w@In-Bi is approximately 45 °C. After 10 s, the surface temperature of GO reached 76.2 °C, whereas that of GO@In-Bi is slightly lower at 74.6 °C. However, the surface temperature of GO_w has increased to 88.2 °C by 15 s, while the temperature of GO_w@In-Bi escalates to 95 °C, significantly higher than that of GO_w. This increase is attributed to the In-Bi alloy becoming liquid at 80 °C and filling the gaps between the material and the heating plate, thereby enhancing interfacial heat transfer and resulting in a more pronounced temperature rise. Fig. 6b shows the corresponding temperature rise curve, which also clearly illustrates this phenomenon. The films are placed between the heating plate and the heat sink to replicate the actual operating conditions of the TIMs and their actual heat dissipation performance is evaluated. The initial temperature of the heating plate is set to 125 °C. The thermal image captured by the infrared camera is presented in Fig. 6c. The left image illustrates the application of GO_w@In-Bi and GO film as

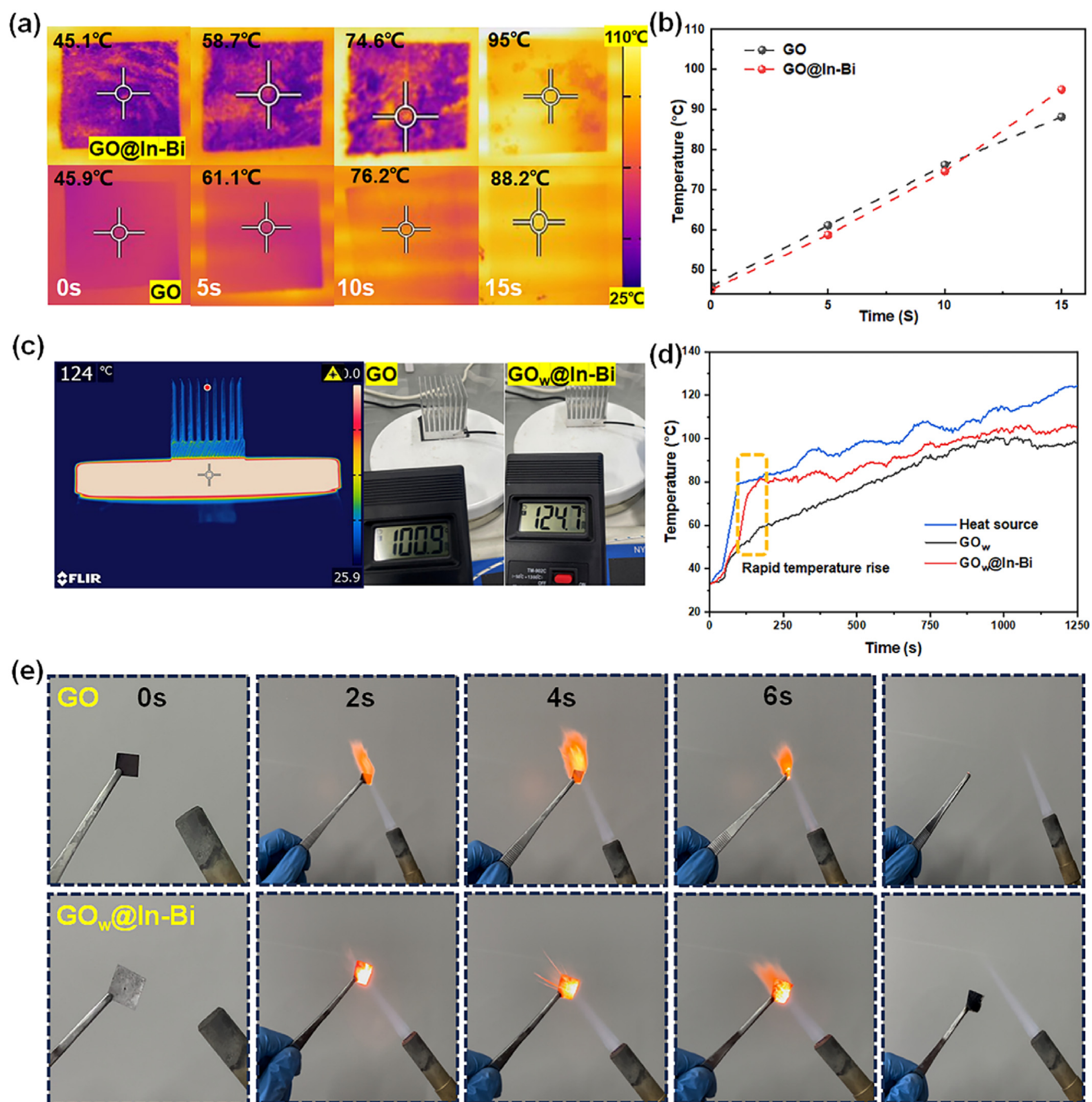

Fig. 6. (a) The surface infrared thermal images of GO$_w$ and GO$_w$@In-Bi by placing them on a heating stage, (b) the corresponding temperature evolution versus time, (c) initial infrared thermal image of the TIMs applied system and the maximum temperature achieved for various incorporated TIMs, (d) the detailed temperature evolution of the heat sinks incorporated with various TIMs, (e) digital images from the flame retardancy test of GO$_w$ and GO$_w$@In-Bi films.

TIMs, while the right image illustrates the schematic diagram of their practical implementation and the temperature of the heat sink after 20 min, recorded by the thermocouple. The heat sink temperature with GO$_w$@In-Bi inserted reaches 124.7 °C, whereas with GO, it is only 100.9 °C. Fig. 6d illustrates the detailed temperature evolution of the heat sinks incorporated with various TIMs. Notably, the heat sink incorporated with GO$_w$@In-Bi exhibits a significant temperature increase after 140 s, when the temperature of the heating platform is approximately 79 °C. This substantial temperature rise can be attributed to the phase transition of the In-Bi alloy, filling the interfacial gap and thereby improving heat transfer efficiency.

The films are subjected to a flame test at 2000 °C to evaluate their flame retardancy, with results presented in Fig. 6e. After a continuous exposure of 6 s, the GO film displays significant decomposition, due to the presence of oxygen-containing functional groups on its surface. In contrast, the GO@In-Bi composite film maintains its original shape, primarily due to the inherent non-combustibility of the liquid metal and its high thermal conductivity, which enables rapid absorption and dispersion of heat from surrounding materials, thus aiding in the reduction of local temperatures and mitigating the propagation of fire. The above analysis proves the excellent thermal performance of the film in practical thermal management applications.

4. Conclusions

In summary, a straightforward and efficient layer-by-layer approach is presented for fabricating GO_w@In-Bi composite films tailored for thermal interfacial applications. The main conclusions are.

(1) the GOw@In-Bi film achieves a cross-plane thermal conductivity of 1.35 W/(m·K) and a low thermal contact resistance of 0.47 °C cm^2/W at 80 °C, benefiting from the phase change of the In-Bi alloy which fills interfacial gaps and enhances contact.
(2) The incorporation of liquid metal and GO provides the film with high flexibility, robust mechanical strength (fracture stress up to 1170.9 kPa), and strong resistance to leakage and deformation.
(3) The composite film demonstrates high thermal stability, low weight loss at elevated temperatures, and survives flame exposure without structural damage.
(4) Infrared thermal imaging and heat dissipation tests confirm the film's superior performance as a TIM, with effective interfacial heat transfer and rapid thermal response.

This study not only presents the fabrication of flexible, leak-proof, and highly thermally conductive GO_w@In-Bi composite films but also systematically analyzes and discusses the properties of thermal interface materials, offering valuable insights for the development and evaluation of liquid metal-based thermal interface materials. Future development directions for In-Bi alloy-based TIMs include enhancing high-temperature stability, improving oxidation resistance, increasing flexibility, reducing costs, and achieving multifunctionality.

CRediT authorship contribution statement

Yifan Li: Writing – review & editing, Writing – original draft, Supervision, Investigation, Data curation, Conceptualization. **Junhui Fan:** Writing – original draft, Methodology, Investigation, Data curation. **Changqing Liu:** Formal analysis, Data curation. **Dahai Zhu:** Writing – review & editing, Validation. **Chen Jiang:** Investigation. **Wei Yu:** Writing – review & editing, Validation, Supervision, Project administration.

Declaration of competing interest

The authors declare that they have no known competing financial interests or personal relationships that could have appeared to influence the work reported in this paper.

Acknowledgments

This work was supported by the National Natural Science Foundation of China (Grant Nos. 52276074, 52306214), the Shanghai Yangfan Program (Grant No. 21YF1414200), the Shanghai Chenguang Plan Program (Grant No. 22CGA78), and the Shanghai Science and Technology Commission Capacity Building Program for Local Institutions (Grant No. 21010500600).

Appendix A. Supplementary data

Supplementary data to this article can be found online at https://doi.org/10.1016/j.tramat.2025.100010.

References

[1] J. Khan, S.A. Momin, M. Mariatti, A review on advanced carbon-based thermal interface materials for electronic devices, Carbon 168 (2020) 65–112, https://doi.org/10.1016/j.carbon.2020.06.012.
[2] C. Zhao, Y. Li, Y. Liu, H. Xie, W. Yu, A critical review of the preparation strategies of thermally conductive and electrically insulating polymeric materials and their applications in heat dissipation of electronic devices, Adv. Compos. Hybrid Mater. 6 (2022) 27, https://doi.org/10.1007/s42114-022-00584-2.
[3] C. Liu, J. Yang, Y. Li, J. Fu, W. Yu, H. Xie, BN green gel thermal interface material with high thermal conductivity and low thermal contact resistance for efficiently thermal management, Surf. Interfaces 47 (2024) 104204, https://doi.org/10.1016/j.surfin.2024.104204.
[4] Y. Zhang, J. Ma, N. Wei, J. Yang, Q. Pei, Recent progress in the development of thermal interface materials: a review, Phys. Chem. Chem. Phys. 23 (2021) 753–776, https://doi.org/10.1039/d0cp05514j.
[5] Z. Xie, Z. Dou, D. Wu, X. Zeng, Y. Feng, Y. Tian, Q. Fu, K. Wu, Joint-inspired liquid and thermal conductive interface for designing thermal interface materials with high solid filling yet excellent thixotropy, Adv. Funct. Mater. 33 (2023) 2370082, https://doi.org/10.1002/adfm.202214071.
[6] K. Hu, D. Chung, Flexible graphite modified by carbon black paste for use as a thermal interface material, Carbon 49 (2011) 1075–1086, https://doi.org/10.1016/j.carbon.2010.10.058.
[7] S. Zheng, H. Xue, Y. Liu, X. Yu, Z. Cao, Alveoli-mimetic synergistic liquid and solid thermal conductive interface as a novel strategy for designing high-performance thermal interface materials, Small 20 (2024) 2306750, https://doi.org/10.1002/smll.202306750.
[8] J. Due, A.J. Robinson, Reliability of thermal interface materials: a review, Appl. Therm. Eng. 50 (2013) 455–463, https://doi.org/10.1016/j.applthermaleng.2012.06.013.
[9] C. Liu, W. Yu, J. Fan, Y. Li, J. Chen, J. Fu, G. Peng, J. Liu, Open package form-stable phase change microspheres with low thermal contact resistance for the thermal management of electronic devices, Appl. Therm. Eng. 241 (2024) 122396, https://doi.org/10.1016/j.applthermaleng.2024.122396.
[10] Z. Zhou, Y. Zhao, Z. Ling, Z. Zhang, W. Lin, X. Fang, Simulative study on the performance of polymeric composites containing phase change capsules for chip heat dissipation, J. Energy Storage 68 (2023) 107851, https://doi.org/10.1016/j.est.2023.107851.
[11] Y. Zhao, Z. Zhang, C. Cai, Z. Zhou, Z. Ling, X. Fang, Vertically aligned carbon fibers-penetrated phase change thermal interface materials with high thermal conductivity for chip heat dissipation, Appl. Therm. Eng. 230 (2023) 120807, https://doi.org/10.1016/j.applthermaleng.2023.120807.
[12] Y. Zhao, Z. Zhang, Z. Ling, X. Gao, X. Fang, Shape-stabilized low melting-point alloy/expanded graphite composite thermal pad with excellent chip heat dissipation performance, Appl. Therm. Eng. 217 (2022) 119202, https://doi.org/10.1016/j.applthermaleng.2022.119202.
[13] Y. Li, H. Lin, N. Mehra, Identification of thermal barrier areas in graphene oxide/boron nitride membranes by scanning thermal microscopy: thermal conductivity improvement through membrane assembling, ACS Appl. Nano Mater. 4 (2021) 4189–4198, https://doi.org/10.1021/acsanm.1c00528.
[14] Y. Zhang, Y. Li, Q. Lei, X. Fang, H. Xie, W. Yu, Tightly-packed fluorinated graphene aerogel/polydimethylsiloxane composite with excellent thermal management properties, Compos. Sci. Technol. 220 (2022) 109302, https://doi.org/10.1016/j.compscitech.2022.109302.
[15] L. Zhang, Y. Li, H. Guo, H. Zhang, N. Zhang, T. Hayat, Y. Sun, Decontamination of U(VI) on graphene oxide/Al_2O_3 composites investigated by XRD, FT-IR and XPS techniques, Environ. Pollut. 248 (2019) 332–338, https://doi.org/10.1016/j.envpol.2019.01.126.
[16] N. Ali, A. Hussain, R. Ahmed, M.F.B. Omar, M. Sultan, Y. Fu, Crystallized $InBiS_3$ thin films with enhanced optoelectronic properties, Appl. Surf. Sci. 436 (2018) 293–301, https://doi.org/10.1016/j.apsusc.2017.11.273.
[17] X. Mao, Y. Li, X. Hu, R. Tian, W. Yu, Expanded graphite (EG)/Ni@ Melamine foam (MF)/EG sandwich-structured flexible bipolar plate with excellent electrical conductivity, mechanical properties, and gas permeability, Appl. Energy 338 (2023) 120929, https://doi.org/10.1016/j.apenergy.2023.120929.
[18] J.M. Ribeiro, F.C. Correia, P.B. Salvador, L. Rebouta, L.C. Alves, E. Alves, N.P. Barradas, A. Mendes, C.J. Tavares, Compositional analysis by RBS, XPS and EDX of ZnO:Al,Bi and ZnO:Ga,Bi thin films deposited by d.c. magnetron sputtering, Vacuum 161 (2019) 268–275, https://doi.org/10.1016/j.vacuum.2018.12.038.
[19] A. Esmaeili, M.H. Entezari, E.K. Goharshadi, Graphene oxide nanosheets synthesized by ultrasound: experiment versus MD simulation, Appl. Surf. Sci. 451 (2018) 112–120, https://doi.org/10.1016/j.apsusc.2018.04.214.
[20] X. Chen, D. Meng, B. Wang, B. Li, W. Li, C.W. Bielawski, R.S. Ruoff, Rapid thermal decomposition of confined graphene oxide films in air, Carbon 101 (2016) 71–76, https://doi.org/10.1016/j.carbon.2016.01.075.
[21] T. Daeneke, K. Khoshmanesh, N. Mahmood, I.A. Castro, D. Esrafilzadeh, S.J. Barrow, M.D. Dickey, K.K. Zadeh, Liquid metals: fundamentals and applications in chemistry, Chem. Soc. Rev. 47 (2018) 4073–4111, https://doi.org/10.1039/c7cs00043j.
[22] E. Jang, D.Y. Ryu, D. Kim, Hydrothermal carbonization improves the quality of biochar derived from livestock manure by removing inorganic matter, Chemosphere 305 (2022) 135391, https://doi.org/10.1016/j.chemosphere.2022.135391.
[23] J. Tao, K. Xu, Y. Wang, L. Xiang, B. Tang, S. Shi, Y. Li, et al., In situ construction of high-thermal-conductivity and negative-permittivity epoxy/carbon fiber@ carbon composites with a 3D network by high-temperature chemical vapor deposition, ACS Appl. Mater. Interfaces 15 (46) (2023) 54027–54038, https://doi.org/10.1021/acsami.3c15040.
[24] C. Wang, S. Tang, X. Liu, G. Su, W. Tian, S. Qiu, Experimental study on heat pipe thermoelectric generator for industrial high temperature waste heat recovery, Appl. Therm. Eng. 175 (2020) 115299, https://doi.org/10.1016/j.applthermaleng.2020.115299.